



Article

# Maize Phenotypic Parameters Based on the Constrained Region Point Cloud Phenotyping Algorithm as a Developed Method

Qinzhe Zhu Miao yuan Bai and Ming Yu \*

College of Computer and Control Engineering, Northeast Forestry University, Harbin 150006, China; zqz061314@gmail.com (Q.Z.); baimy@nefu.edu.cn (M.B.)

\* Correspondence: yuming@nefu.edu.cn

**Abstract:** As one of the world's most crucial food crops, maize plays a pivotal role in ensuring food security and driving economic growth. The diversification of maize variety breeding is significantly enhancing the cumulative benefits in these areas. Precise measurement of phenotypic data is pivotal for the selection and breeding of maize varieties in cultivation and production. However, in outdoor environments, conventional phenotyping methods, including point cloud processing techniques based on region growing algorithms and clustering segmentation, encounter significant challenges due to the low density and frequent loss of point cloud data. These issues substantially compromise measurement accuracy and computational efficiency. Consequently, this paper introduces a Constrained Region Point Cloud Phenotyping (CRPCP) algorithm that proficiently detects the phenotypic traits of multiple maize plants in sparse outdoor point cloud data. The CRPCP algorithm consists primarily of three core components: (1) a constrained region growth algorithm for effective segmentation of maize stem point clouds in complex backgrounds; (2) a radial basis interpolation technique to bridge gaps in point cloud data caused by environmental factors; and (3) a multi-level parallel decomposition strategy leveraging scene blocking and plant instances to enable high-throughput real-time computation. The results demonstrate that the CRPCP algorithm achieves a segmentation accuracy of 96.2%. When assessing maize plant height, the algorithm demonstrated a strong correlation with manual measurements, evidenced by a coefficient of determination  $R^2$  of 0.9534, a root mean square error (RMSE) of 0.4835 cm, and a mean absolute error (MAE) of 0.383 cm. In evaluating the diameter at breast height (DBH) of the plants, the algorithm yielded an  $R^2$  of 0.9407, an RMSE of 0.0368 cm, and an MAE of 0.031 cm. Compared to the PointNet point cloud segmentation method, the CRPCP algorithm reduced segmentation time by more than 44.7%. The CRPCP algorithm proposed in this paper enables efficient segmentation and precise phenotypic measurement of low-density maize multi-plant point cloud data in outdoor environments. This algorithm offers an automated, high-precision, and highly efficient solution for large-scale field phenotypic analysis, with broad applicability in precision breeding, agronomic management, and yield prediction.



**Citation:** Zhu, Q.; Bai, M.; Yu, M. Maize Phenotypic Parameters Based on the Constrained Region Point Cloud Phenotyping Algorithm as a Developed Method. *Agronomy* **2024**, *14*, 2446. <https://doi.org/10.3390/agronomy14102446>

Academic Editor: Luís Manuel Navas Gracia

Received: 11 July 2024

Revised: 28 August 2024

Accepted: 14 October 2024

Published: 21 October 2024



**Copyright:** © 2024 by the authors. Licensee MDPI, Basel, Switzerland. This article is an open access article distributed under the terms and conditions of the Creative Commons Attribution (CC BY) license (<https://creativecommons.org/licenses/by/4.0/>).

## 1. Introduction

As one of the world's three principal food crops, maize is extensively cultivated across the globe [1]. Cultivating high-yield, disease-resistant, and superior-quality maize varieties can significantly boost food production and quality. This is achieved through optimized genetic selection and refined cultivation practices, effectively easing the food demand pressures from population growth and enhancing global food security [2]. Accurate phenotypic data are crucial for identifying desirable traits and speeding up variety improvement, providing the scientific basis to achieve these goals [3,4]. Therefore, rapidly and accurately acquiring phenotypic data is essential in maize breeding. Traditional phenotypic measurement methods mainly rely on direct observation and measurement of

morphological traits like plant height and leaf size. Although intuitive, these methods are time-consuming, labor-intensive, and prone to human error. With rapid advances in remote sensing technology and computer systems, the early 21st century saw the use of LiDAR, high-resolution cameras, and multispectral imagers in crop data collection. The high-precision 3D point clouds and multi-source image data from these advanced devices, when processed through sophisticated computational techniques, enable efficient, non-invasive, and rapid measurement of crop phenotypic parameters, providing strong technical support for precision agriculture and crop breeding [5]. In recent years, the rapid development of 3D reconstruction technology has enabled the fast collection of data and extraction of phenotypes in three-dimensional space (Yang et al. [6]). Currently, 3D reconstruction technologies for plant phenotyping include LiDAR, stereo cameras, time-of-flight (TOF) cameras, and structure from motion (SfM) [7,8].

LiDAR provides high spatial resolution, operates in all weather conditions, and benefits from multi-source data fusion, ensuring superior measurement accuracy. Hu et al. [9] used multi-sensor fusion techniques that integrated LiDAR and depth cameras. They applied the equidistant extension polygon algorithm and the FILL-DBSCAN clustering algorithm to achieve high-precision recognition and distance measurement of maize leaves and stems. Zhao et al. [10] extracted maize plant height information from multi-angle point cloud data using solid-state LiDAR, combined with supervoxel clustering and Euclidean distance algorithms.

Despite the clear advantages of 3D LiDAR scanning, its application is limited by high cost, complex data processing, bulky equipment, strict environmental requirements, and challenges in data interpretation. With the advancement of depth camera technology, Kim et al. [11] used a simple binocular camera to capture images and applied machine vision algorithms to automatically segment crop areas and estimate crop height. The ToF camera is an active sensor that emits modulated near-infrared light. It measures the time taken for the light to reach and return from each scene point, calculates the distance to the camera, and acquires depth data beneath the crop canopy [12]. Structured light sensors have significant advantages in measuring plant parameters, including real-time capability, efficiency, and low cost. Xu et al. [13] used a Kinect sensor to acquire multi-view data of maize populations and achieved global 3D reconstruction using iterative algorithms to measure crop phenotypic characteristics on the reconstructed 3D models. Azzari et al. [14] used the Kinect depth sensor for non-destructive 3D scanning and modeling. They cross-validated the results with traditional manual measurements and developed a novel method for rapidly measuring vegetation structure and biomass. These depth-sensing data collection methods are cumbersome and unsuitable for outdoor environments with intense light. Additionally, the measurement range is limited to a few meters due to the sensor's low resolution.

As machine vision and deep learning technologies continuously advance, more intelligent measurement methods are being developed. Yang et al. [15] used a physics-based elastic deformation framework combined with the PointNet++ model and the finite element method to enhance maize point cloud data, achieving precise segmentation of maize stems and leaves. Gao et al. [16] used the YOLOv7-SlimPose model with a binocular stereo camera to efficiently extract maize phenotypic parameters through keypoint detection and depth map generation. Yang et al. [17] developed a precise evaluation framework for maize ear rot disease using 3D point clouds, integrating the ERSegNet network with a direction coding module and a point transformation attention module, achieving accurate measurement of maize ear phenotypic parameters.

Despite the progress made in extracting phenotypic traits of maize plants, challenges remain in simultaneously segmenting multiple maize plants from low-density point cloud data: (1) In outdoor environments, factors like lighting and vegetation cover can result in low-density maize point cloud data. This makes it difficult for segmentation algorithms to accurately identify and segment individual maize plants, as the data may lack sufficient detail to precisely define each plant's boundaries and structural characteristics [18,19].

(2) Mutual occlusion between plants during data collection often leads to missing or noisy point cloud data. These incomplete and inaccurate data reduce the segmentation algorithm's ability to fully capture the morphological characteristics of individual plants, affecting the accuracy and completeness of the segmentation [20,21]. (3) In maize fields, complex backgrounds and environmental interferences, such as weeds and soil, can blend with maize plants. This complicates the task for segmentation algorithms, making it difficult to distinguish between plant boundaries and the background, thereby impacting segmentation accuracy and stability [22,23]. (4) While deep learning methods can achieve high segmentation accuracy, they require substantial data and difficult parameter tuning, leading to low computational efficiency in practical applications. The current 3D plant segmentation datasets are limited in size, posing significant challenges in meeting the training needs of high-quality deep learning models. Particularly for field crops like maize, with complex morphological features, irregular leaf shapes, and intricate leaf-stem connections, deep learning-based methods often struggle to maintain segmentation accuracy while processing efficiently [24,25]. This challenge is especially pronounced in scenarios requiring real-time or large-scale point cloud data processing.

To address these challenges, this study introduces the Constrained Region Point Cloud Phenotyping (CRPCP) algorithm. (1) The constrained region growth algorithm segments the maize point cloud data in complex backgrounds, efficiently isolating the point cloud of maize plant stems. (2) Radial basis interpolation is applied to the segmented stem point clouds to compensate for data loss caused by environmental factors (e.g., occlusion, sensor failure), resulting in more complete plant point cloud data. (3) The algorithm employs a multi-level parallel decomposition strategy, based on scene partitioning and plant instances, to achieve high-throughput real-time computation. Ultimately, through segmentation, completion, and parallel computation, the CRPCP algorithm accurately isolates each maize plant's complete 3D point cloud model from complex field environments, providing a foundation for subsequent phenotypic parameter extraction. This study aims to (1) employ robust methods for acquiring, denoising, separating ground points, and cropping field maize point cloud data in outdoor settings; (2) develop the CRPCP algorithm to enable efficient and high-precision measurement of key phenotypic parameters (plant height, stem diameter) of multiple maize plants in complex outdoor environments; and (3) validate the algorithm's applicability and stability across various growth stages and maize varieties.

The CRPCP algorithm proposed in this study introduces a significant innovation in handling low-density point cloud data with gaps and complex backgrounds in outdoor environments. Unlike deep learning approaches that require large-scale annotated datasets and extensive computational resources, the CRPCP algorithm integrates geometric constraints with mathematical modeling, significantly enhancing computational efficiency while maintaining high precision. This approach is particularly well suited for real-time analysis of field crops with complex morphology, such as maize. The algorithm addresses the limitations of existing methods in outdoor settings and provides a rapid, precise solution for large-scale field maize phenotypic analysis. The innovative CRPCP methodology offers new insights into phenotypic measurement for other crops, with significant scientific and practical implications for advancing precision agriculture and crop breeding.

## 2. Materials and Methods

### 2.1. Test Site

The experimental site was the Yonghe Vegetable Company maize base (Binxi, Harbin, Heilongjiang Province, China), characterized by a temperate continental monsoon climate. The average daily temperatures from May to July 2023 were 14 °C, 20.5 °C, and 24.5 °C. The maize variety tested was Jiyu 335, planted at a density of 82,500 plants per hectare. Sowing was performed manually on 8 May 2023, with a row spacing of 45 cm and a plant spacing of 10 cm. Sowing, harvesting, and field management followed local conventional practices. The experimental varieties and agronomic parameters, including

planting density, were provided by Yonghe Vegetables Co., Ltd., and align with local maize cultivation practices.

## 2.2. Data Acquisition

In this study, the Pegasus SLAM-100 handheld LiDAR was used during the maize tasseling stage to acquire high-quality 3D point cloud data, with an average plant height of 180 cm at the time of collection. The device is equipped with 16 transmit/receive channels, offering a 270° horizontal field of view, a 360° vertical field of view, a maximum range of 120 m, and a resolution of 1 cm. During operation, the 905 nm wavelength laser collects 3D positional data of target objects using a 360-degree omnidirectional scanning method. The LiDAR was positioned at the center of the field at a height of 1.5 m. Using horizontal and vertical rotating scanning mechanisms; it sampled surrounding plants from multiple angles without blind spots, ensuring comprehensive plant point cloud data, as shown in Figure 1a.

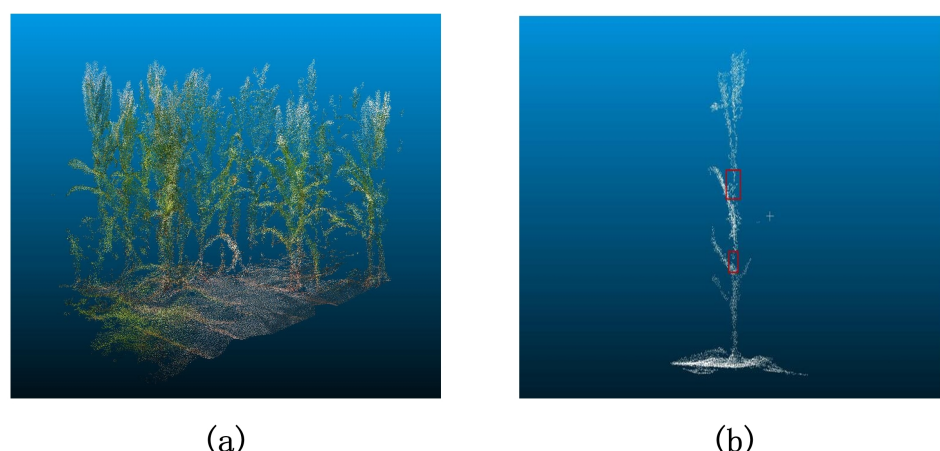


**Figure 1.** (a) The three-dimensional point cloud data of corn plants and (b) low-density single corn plant point cloud, with the red box indicating regions of sparse data due to occlusion and missing points.

Despite the excellent performance of the collection equipment, the point cloud data obtained in the complex outdoor environment still showed low density and data loss. Due to dense maize plants and the occlusion of leaves and stems, the collected point cloud data contained many voids and missing areas, resulting in low point cloud density [26]. Figure 1b shows an example of low-density point cloud data of a single maize plant, where the distribution is sparse with significant gaps. Ultimately, we acquired a maize plant point cloud dataset with approximately 170,000 data points, which is sparse compared to traditional high-density datasets. To address the challenges of measuring phenotypic parameters from low-density, incomplete point cloud data, this paper proposes the CRCP algorithm, which effectively manages sparse data and provides an innovative solution for precise maize phenotypic measurement.

## 2.3. Point Cloud Data Preprocessing

### 2.3.1. Noise Removal

To ensure accurate 3D reconstruction, the Voxel Grid Filtering algorithm was used to preprocess noise in the raw point cloud data. The algorithm denoises by mapping the point cloud onto a regular 3D voxel grid, replacing multiple points within the same voxel with their centroid. This process effectively minimizes background noise and outliers while preserving the geometric structure of the point cloud [27,28]. Voxel grid filtering offers high computational efficiency and straightforward parameter determination, making it ideal for processing large-scale, complex point cloud data. In this study, voxel cubes with a side length of 3 mm were used, reducing the number of point clouds by approximately

50% after noise reduction. The principle of the voxel grid filtering algorithm is shown in Figure 2.

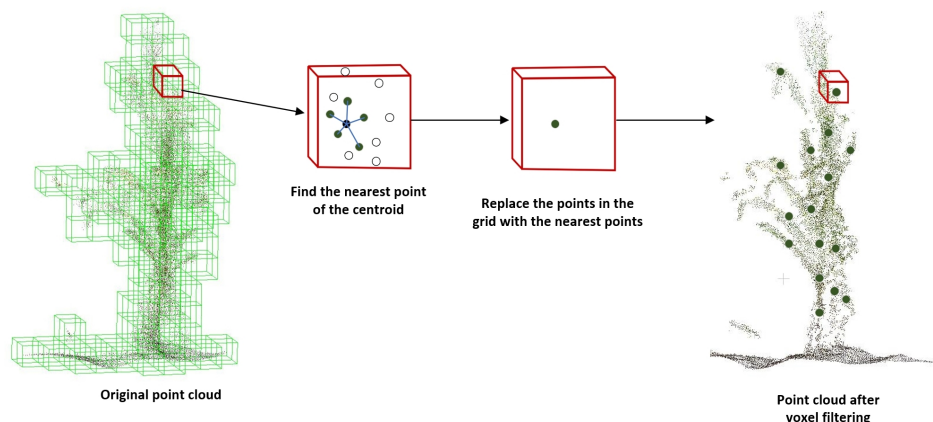


**Figure 2.** A schematic diagram of the principle of the voxel denoising algorithm.

### 2.3.2. Separation of Ground and Non-Ground Points

Separating ground points is a crucial preprocessing step in 3D plant reconstruction. This study employed an enhanced RANSAC (Random Sample Consensus) algorithm to differentiate non-ground points from complex maize plant point cloud data. The algorithm fits a plane model iteratively by randomly selecting a subset of points from the point cloud data. For each candidate plane, distances of all points to the plane are calculated, and points are classified as inliers (ground points) or outliers (non-ground points) based on a predefined threshold. After multiple iterations, the plane with the most inliers is chosen as the optimal model, effectively identifying and separating ground points [29,30]. The main advantage of this algorithm is its robust resistance to noise and outliers, making it ideal for processing complex plant point cloud data with numerous outliers. Figure 3 illustrates the effectiveness of this algorithm in separating ground points. This algorithm successfully extracted non-ground point clouds from the original plant point cloud, effectively reducing ground-induced plant occlusion.

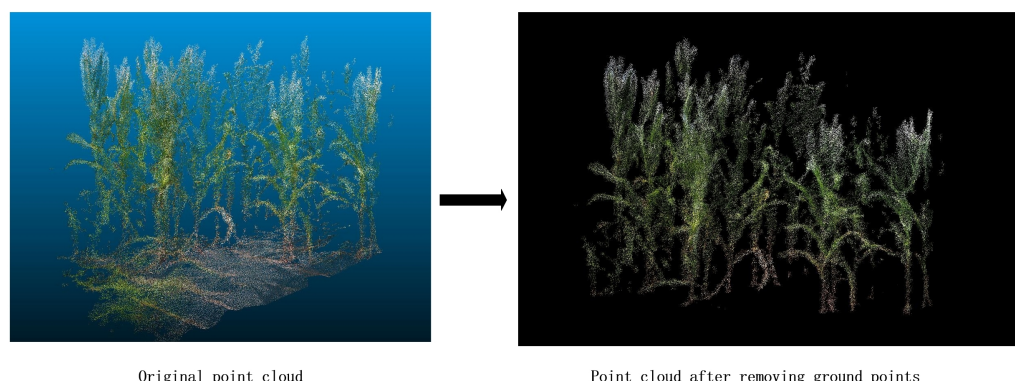


**Figure 3.** Ground point separation schematic diagram.

### 2.3.3. Point Cloud Cropping

This study used CloudCompare version 2.11.0 to crop non-ground point clouds after removing ground points, extracting point cloud data for individual maize plants and groups of three. Figure 4a shows the cropped point cloud data of a single maize plant, used to illustrate the subsequent algorithm process and parameter settings. Figure 4b shows the point cloud data of three maize plants, used to validate the algorithm's efficacy in a densely planted environment.

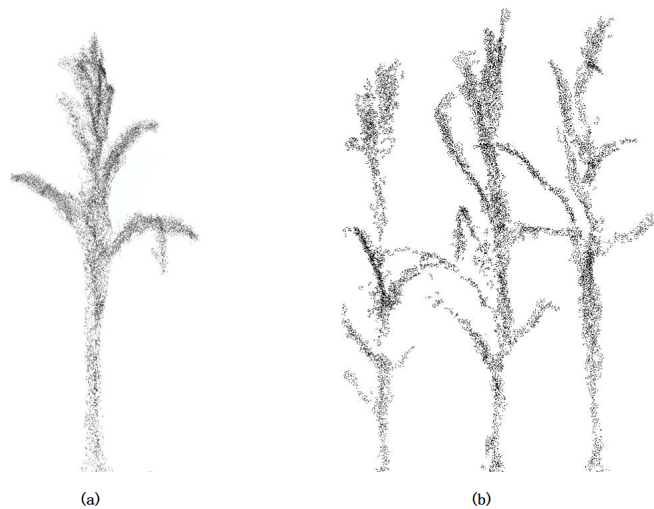


**Figure 4.** (a) Single corn plant point cloud data and (b) Point cloud data of three corn plants.

#### 2.4. Stem Segmentation

This paper introduces the stem segmentation component of the CRPCP algorithm, designed to accurately and efficiently segment the stem point cloud of individual maize plants from low-density point cloud data in complex field environments. The CRPCP algorithm for segmenting maize stem point clouds involves four main steps: constrained region growth, elimination of over-segmented points based on central axis distance, adaptive parameter adjustment, and multi-parameter cyclic optimization. The constrained region growth algorithm segments the initial stem point cloud efficiently using parallel growth and dynamic region merging strategies. Over-segmented points are removed based on the central axis distance to optimize segmentation. Adaptive adjustments of the growth radius, weights, and other parameters improve segmentation quality. Multi-parameter cyclic processing thoroughly segments the complex plant structure. The CRPCP algorithm's segmentation process is shown in Figure 5.

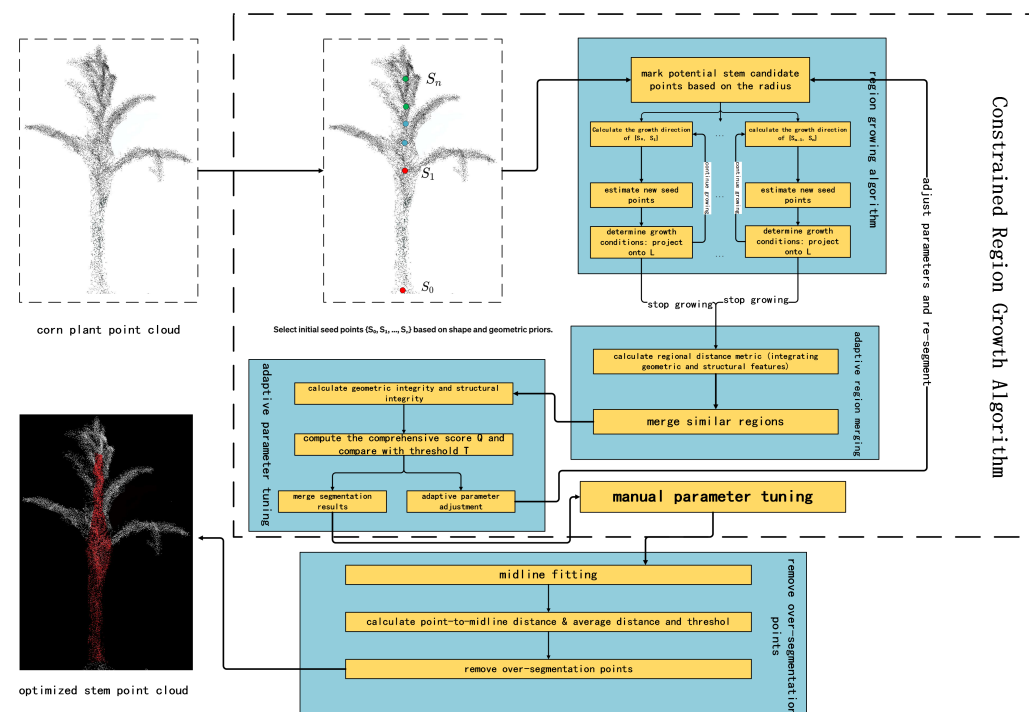


**Figure 5.** CRPCP algorithm for segmentation of maize stem point cloud segmentation process, with arrows illustrating the segmentation workflow.

#### 2.4.1. Constrained Region Growth Algorithm

By adjusting the parameters  $s_0, s_n, r_1, M$ , the trade-off between segmentation quality and efficiency in the constrained region growing algorithm can be managed. The settings for  $s_0$  and  $s_n$  dictate the starting point and direction of growth, crucial for effectively covering critical stem regions. A well-chosen starting point and direction enhance segmentation accuracy and minimize redundant computations, optimizing overall efficiency. The parameter  $r_1$  controls the radius of the initial growth sphere, directly affecting segmentation granularity. A smaller  $r_1$  captures detailed local structures but may lead to over-segmentation, while a larger  $r_1$  produces coarser segmentation, helping to avoid omitting key features. The parameter  $M$  determines the maximum number of growth steps, thereby controlling the growth process duration. A larger  $M$  extends the growth process, ensuring comprehensive coverage of the stem region and preventing premature termination. In contrast, a smaller  $M$  enhances computational efficiency by shortening the growth process and reducing unnecessary calculations.

Step 1: Utilizing morphological and geometric prior knowledge, select multiple sets of starting points  $s_0, s_1, \dots, s_n$ , ensuring each starting point is located in the stem region and covers various structural positions. For each  $s_i$ , employ a sphere  $B(s_i, r_1)$  with radius  $r_1$  to initially designate all points within it as potential stem point candidates  $P_{0,i}$ .

#### Step 2: Multi-Region Parallel Growth

For each starting point  $s_{0,i}$  and its corresponding candidate set  $P_i$ , independently perform region growth according to steps 2a–2c to obtain multiple growth regions  $R_1, R_2, \dots, R_n$ .

##### a: Growth Direction Calculation

Based on the current candidate set  $P_k$ , calculate the growth direction vector  $v_k$ :

$$\bar{v}_1 = \begin{cases} \frac{\sum_{p \in P_k} w_p \frac{p - s_k}{|p - s_k|}}{\sum_{p \in P_k} w_p}, & P_k \neq \emptyset \\ 0, & P_k = \emptyset \end{cases} \quad (1)$$

$$v_k = \alpha \cdot \bar{v}_1 + \beta \cdot \frac{s_n - s_k}{|s_n - s_k|} \quad (2)$$

where  $\bar{v}_1$  is the weighted vector average of all  $v_{1,i}$ , with the weight  $w_p$  determined by geometric attributes such as point density and curvature, reflecting the overall directional trend of local stem points.  $v_k$  is the final growth direction vector, with  $\alpha$  and  $\beta$  controlling the influence weights of both factors. In practice,  $w_p = 0.6$ ,  $\alpha = 0.2$ , and  $\beta = 0.8$ .

##### b: Estimate the new seed point position:

$$s_{k+1} = s_k + r_1 \cdot v_k \quad (3)$$

where  $r_1$  is the sphere radius for searching neighboring points, controlling the step size for each iteration.

c: Determine the growth termination condition: calculate the projection point  $\text{proj}_L(s_{k+1})$  of  $s_{k+1}$  on the predefined line  $L$  and the projection parameter  $t_{\text{proj}}$ :

$$\text{proj}_L(s_{k+1}) = s_0 + \frac{(s_{k+1} - s_0) \cdot (s_n - s_0)}{|s_n - s_0|^2} (s_n - s_0) \quad (4)$$

$$t_{\text{proj}} = \frac{(s_{k+1} - s_0) \cdot (s_n - s_0)}{|s_n - s_0|^2} \quad (5)$$

If  $0 \leq t_{\text{proj}} \leq 1$ , then  $\text{proj}_L(s_{k+1})$  is on the line segment  $L$ , and the region  $R_k$  continues to grow; otherwise, the growth of  $R_k$  terminates.

### Step 3: Dynamic Region Merging Strategy

a: Region Distance Measure. To measure the similarity between two regions  $R_i$  and  $R_j$ , a distance measure is defined that combines geometric and structural features:

$$d(R_i, R_j) = w_1 \cdot d_c(c_i, c_j) + w_2 \cdot d_e(e_i, e_j) + w_3 \cdot d_p(P_i, P_j) \quad (6)$$

Among them  $w_1, w_2, w_3$  are the weight coefficients for the centroid distance  $d_c(c_i, c_j)$ , endpoint distance  $d_e(e_i, e_j)$ , and point cloud distance  $d_p(P_i, P_j)$ . The centroid distance  $d_c(c_i, c_j)$  reflects the positional differences in the stem structure between the two regions; the endpoint distance  $d_e(e_i, e_j)$  calculates the consistency in shape direction between the two regions; the point cloud distance  $d_p(P_i, P_j)$  calculates the distance between the two point cloud sets. In practice,  $w_1 = 0.3, w_2 = 0.3, w_3 = 0.4$ .

b: Define the Geometric Integrity Evaluation  $Q_g$  and Structural Integrity Evaluation  $Q_s$ :

$$\begin{aligned} Q_g &= w_1 \cdot C_{\text{curv}} + w_2 \cdot C_{\text{density}} \\ &= w_1 \cdot \frac{1}{N} \sum_{i=1}^N \left( \frac{1}{1 + |\kappa_i - \bar{\kappa}|} + \lambda_\kappa \exp(-\beta_\kappa |\Delta \kappa_i|) \right) \\ &\quad + w_2 \cdot \frac{1}{N} \sum_{i=1}^N \left( \frac{1}{1 + |\rho_i - \bar{\rho}|} + \lambda_\rho \exp(-\beta_\rho |\Delta \rho_i|) \right) \end{aligned} \quad (7)$$

$$Q_s = w_3 \cdot \left( 1 - \frac{N_{\text{outlier}}}{N_{\text{total}}} \right) + w_4 \cdot \left( 1 - \frac{1}{N_R} \sum_j \frac{d_j}{d_{\max}} \right) \quad (8)$$

where  $w_1, w_2, w_3, w_4$  are the weight coefficients for the curvature, density consistency, outlier ratio, and average distance;  $\kappa_i, \bar{\kappa}$  are the point curvature values, with their differences reflecting curvature consistency;  $\lambda_\kappa, \beta_\kappa$  control the shape of the curvature consistency term, adjusting sensitivity to curvature differences;  $\rho_i$  is the point density;  $\lambda_\rho, \beta_\rho$  control the shape of the density consistency term;  $N, N_{\text{outlier}}, N_{\text{total}}$  are the total number of points within the region, the number of outliers, and the total number of points;  $d_j$  is the distance from the  $j$ -th point to the centroid.

Comprehensive Evaluation Score:

$$Q = \alpha Q_g + \beta Q_s \quad (9)$$

### c: Adaptive Merging Threshold

The initial merging threshold  $\tau_0$  is established at the 85th to 90th percentile of the distance distribution, effectively encompassing most similar region pairs while excluding some extreme outliers. This is further optimized via an adaptive adjustment strategy:

$$\tau_{t+1} = (1 - \eta) \tau_t + \eta f(Q_t, T) \quad (10)$$

When  $d(R_i, R_j) < \tau_t$ ,  $R_i$  and  $R_j$  are merged into  $R_k = R_i \cup R_j$ .

### d: Adaptive Adjustment Parameters

When  $Q < T$ , adaptively adjust the parameters  $\{r_1, M, \alpha, \beta\}$ :

$$r_1^{(t+1)} = r_1^{(t)} \cdot \left( 1 + \lambda_r (T - Q^{(t)}) \right) \quad (11)$$

$$M^{(t+1)} = M^{(t)} \cdot \left( 1 + \lambda_M (T - Q^{(t)}) \right) \quad (12)$$

$$\alpha^{(t+1)} = \alpha^{(t)} + \eta_\alpha \frac{\partial Q}{\partial \alpha} \quad (13)$$

$$\beta^{(t+1)} = \beta^{(t)} + \eta_\beta \frac{\partial Q}{\partial \beta} \quad (14)$$

Here,  $r_1$  denotes the initial sphere radius;  $\lambda_r$  represents the adaptive step size control parameter for  $r_1$ ;  $\eta_\alpha$  and  $\eta_\beta$  are the adaptive step size control parameters for  $\alpha$  and  $\beta$ , respectively;  $Q^{(t)}$  is the comprehensive evaluation score for the  $t$ -th iteration;  $T$  is the target quality score threshold.

When  $Q \geq T$ , the parameters remain unchanged. Manual fine-tuning of the parameters is supported to further optimize the segmentation outcome.

Step 4: For complex plant structures, the algorithm employs multiple sets of parameters ( $s_0, s_n, r_1, M$ ) for segmentation. Upon completing the segmentation with a single set, the results are consolidated to form the current model; the consolidated model is then evaluated to identify any regions that were inaccurately segmented. If the segmentation is deemed unsatisfactory, the parameter sets are adjusted according to the evaluation to address the missegmented areas. The segmentation and consolidation steps are iterated until the entire model is satisfactory. By processing with multiple sets of parameters cyclically, local regions can be optimized in stages, thereby achieving comprehensive segmentation of complex plants.

#### 2.4.2. Removal of Over-Segmented Points Based on Midline Distance

In our research on the segmentation of corn plant point clouds, a crucial step is the removal of over-segmented points to enhance the accuracy of stem extraction. To this end, we implemented a ‘stem central axis fitting’ algorithm, which posits that the stem extends along a principal axis, using this axis to characterize the stem’s overall geometric features. This algorithm effectively captures the central axis of the stem, offering a precise reference for subsequent distance calculations and point cloud optimization, enabling the more accurate identification and removal of over-segmented points.

Step 1: Midline Fitting: For the stem data in the point cloud, fit the midline using the stem axial model:

$$L(t) = \vec{p} + t\vec{d} \quad (15)$$

where  $\vec{p}$  represents any point on the line,  $\vec{d}$  is the direction vector, and  $t$  is the parameter.

Step 2: Calculate Distance: For each point  $P(x_i, y_i, z_i)$  in the point cloud, compute the minimum Euclidean distance to the midline  $L$  as the distance  $D_i$ :

$$D_i = \min |P - (\vec{p} + t\vec{d})| \quad (16)$$

Step 3: Average Distance and Threshold Setting: Define the average distance of all points to the midline  $\bar{D}$  and set the threshold  $\tau = k\bar{D}$ , where  $k$  is a factor adjusted based on the data. By defining the average distance of all points to the midline and establishing a threshold based on this average distance, over-segmented points can be identified.

Step 4: Removal Process: If the distance  $D_i$  of point  $P_i$  to the midline exceeds the threshold  $\tau$ , then  $P_i$  is considered an over-segmented point and is removed from the dataset.

Through the aforementioned steps, points that do not belong to the stem structure can be effectively removed, thereby providing a more accurate data foundation for the subsequent extraction of phenotypic parameters of corn plants.

#### 2.5. Radial Basis Function-Based Constrained Adaptive Point Cloud Completion

To address the challenge of missing maize plant point cloud data in complex environments and achieve a more complete 3D point cloud model, this paper introduces the point cloud completion component of the CRPCP algorithm. Radial Basis Function (RBF) interpolation was used for data completion. The RBF interpolation method offers exceptional smoothness and stability when processing irregular and sparse point cloud data, effectively addressing model discontinuities due to data loss while preventing artifacts and errors in handling local geometric complexities. Stem point cloud completion using the CRPCP algorithm involves several key steps: extracting data from the original point cloud, fitting a cylindrical model to determine geometric coefficients, estimating the expected number of interpolated points based on regional attributes and color, generating a completed point

cloud object, and finally, performing bilateral filtering, smoothing, and topological repair. The CRPCP algorithm's completion process is illustrated in Figure 6.

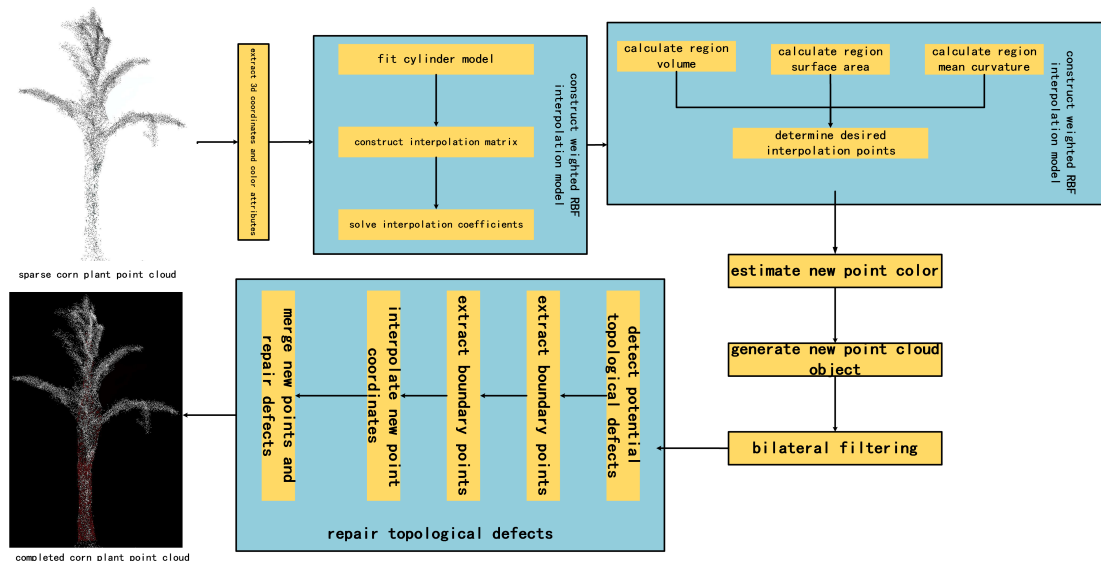


**Figure 6.** CRPCP algorithm segmentation of corn stalk point cloud completion procedure, with arrows illustrating the completion process.

Step 1: Point Cloud Data Extraction. Extract the three-dimensional spatial coordinates and color attributes of each point in the corn stem point cloud. The point cloud coordinates and color can be represented as follows:

$$\{(x_i, y_i, z_i, \text{color}_i)\}_{i=1}^N \quad (17)$$

where  $(x_i, y_i, z_i)$  denotes the spatial coordinate of the  $i$ -th point,  $\text{color}_i$  is the corresponding color attribute, typically an RGB triplet, and  $N$  is the total number of points in the point cloud.

Step 2: Interpolation Model Construction. Utilizing robust techniques such as RANSAC, an approximate cylindrical model is fitted from the stem point cloud, with its axis equation represented as follows:

$$z = f(x, y) = ax + by + c \quad (18)$$

A weighted Gaussian function  $\phi(r) = \exp\left(-\frac{(\epsilon r)^2}{w_i}\right)$  is chosen as the RBF basis function, where  $w_i = \frac{1}{\rho_i} = \frac{1}{\frac{k}{\pi r^k}}$  represents the adaptive weight of the  $i$ -th point, inversely proportional to the point cloud density  $\rho_i$ . Construct the weighted interpolation matrix as follows:

$$A_{ij} = w_i w_j \phi(|p_i - p_j|) \quad (19)$$

After incorporating prior constraints, the linear equation becomes

$$z'_i = \alpha z_i + (1 - \alpha)f(x_i, y_i) \quad (20)$$

$$\sum_{j=1}^N \lambda_j A_{ij} = z'_i \quad (21)$$

Solve for the interpolation coefficients  $\lambda$ .

**Step 3: Regional Adaptive Interpolation.** Introduce the regional volume  $V_m$ , surface area  $A_m$ , and average curvature  $\kappa_m$  to determine the expected number of interpolation points  $N_m$  for each region as follows:

$$N_m = N_0 \cdot (\alpha_m \frac{V_m}{V_0} + \beta_m \frac{A_m}{A_0} + \gamma_m \kappa_m) \quad (22)$$

where  $\alpha_m, \beta_m, \gamma_m$  are the corresponding weight coefficients, adjustable according to actual requirements.

**Step 4: Color Estimation Strategy.** Utilize the neighborhood weighted average to estimate the color of new interpolation points as follows:

$$\text{color}'_j = \sum_{k=1}^K w_k \text{color}_{\text{neighbor},k} \quad (23)$$

Here,  $K$  represents the number of neighborhood points, and  $w_k$  denotes the corresponding weight. This strategy ensures smooth color transitions, thereby avoiding visual distortion.

**Step 5: Generation of New Point Cloud Object.** Merge the original point cloud with the new interpolation points to generate a complete and refined point cloud model as follows:

$$\{\mathbf{x}_i\}_{i=1}^{N+M} = \{(x_i, y_i, z_i)\}_{i=1}^N \cup \{(x_j, y_j, z'_j)\}_{j=1}^M \quad (24)$$

**Step 6: Smoothing and Topological Repair.** Apply bilateral filtering to the new point cloud to effectively denoise while preserving details as follows:

$$\mathbf{p}_i = \frac{1}{W_p} \sum_{\mathbf{p}_j \in \Omega_{\mathbf{p}_i}} G_{\sigma_s}(|\mathbf{p}_i - \mathbf{p}_j|) G_{\sigma_r}(|I_i - I_j|) \mathbf{p}_j \quad (25)$$

Here,  $\Omega_{\mathbf{p}_i}$  denotes the neighborhood of  $\mathbf{p}_i$ ;  $G_{\sigma_s}$  and  $G_{\sigma_r}$  are the spatial and attribute weight kernels, respectively;  $I_i$  represents the attribute of  $\mathbf{p}_i$  (e.g., color, normal vector, etc.). Detect potential topological defect regions  $\Omega_k$  in the completed point cloud. For each  $\Omega_k$ , extract the boundary point set  $\mathbf{q}_i | i = 1^M$ ; uniformly sample the interpolation point set  $\mathbf{p}_j | j = 1^L$  within  $\Omega_k$ ; use weighted RBF interpolation to calculate the coordinates of new interpolation points as follows:

$$z'_{\mathbf{p}_j} = \sum_{i=1}^M w_i \lambda_i \phi(|\mathbf{p}_j - \mathbf{q}_i|) \quad (26)$$

Incorporate the new points into  $\Omega_k$  to repair defects, ensuring the overall point cloud topology is reasonable.

## 2.6. Parallel Computing Strategies and Optimization

To meet the demand for high-throughput point cloud segmentation, completion, and feature extraction of maize plants in field environments, and to enhance overall processing throughput, this paper introduces a parallel computing strategy based on scene partitioning and plant instances, incorporating optimizations such as thread block data sharing for the GPU kernel.

### 2.6.1. Synchronized Incremental Segmentation and Completion Process

An initial completion model is constructed based on the seed point set. Then, region-growing segmentation and local interpolation updates are performed simultaneously, followed by region merging. Finally, over-segmented points are removed, and topological repairs are made to generate a refined and complete final model. The advantages of this improvement are manifold: Pre-implementing global completion establishes a more robust

foundational model for subsequent segmentation and incremental completion. The entire process of segmentation growth and local incremental interpolation is tightly integrated, enabling real-time updates of the overall model and interpolation matrix, thus avoiding redundant intermediate steps. The merging operation is conducted after segmentation and incremental completion, ensuring the model is up-to-date and complete without requiring additional completion. Finally, topological detection and repair are conducted to ensure the completeness and integrity of the final model. The detailed process is illustrated in Figure 7.

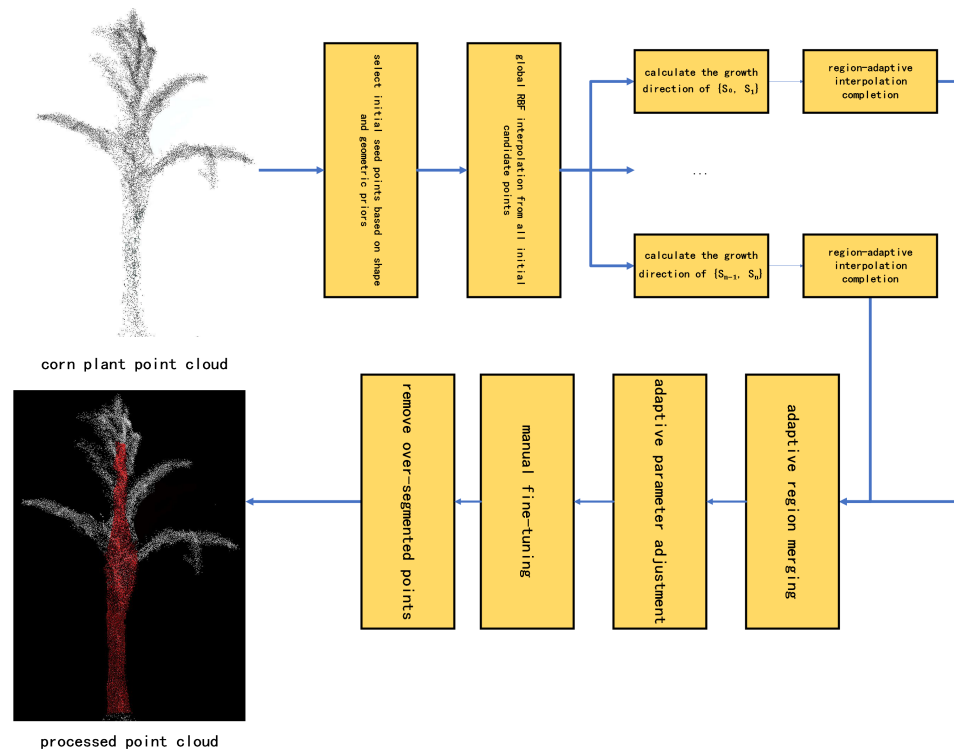


**Figure 7.** Schematic diagram of the synchronous incremental segmentation completion process, with arrows indicating the key steps in the process.

#### 2.6.2. Heterogeneous Parallel Computing Strategy Based on Scene Blocking and Plant Instances

A heterogeneous parallel computing strategy based on scene blocking and plant instances is employed. This strategy utilizes a two-level parallel approach, efficiently leveraging CPU and GPU heterogeneous systems for vegetation modeling and analysis. At the first level, multiple threads are initiated on the host side, each handling the point cloud data of a scene block. Based on characteristics such as point density and plant count, the optimal CUDA thread grid configuration is calculated, and a corresponding number of CUDA streams are initiated to execute kernel computations in parallel on the GPU. At the second level, each thread in the GPU kernel calculates the plant instance ID based on its unique global index, reading and processing only the point cloud data for that plant. The threads share data within the thread block to execute core algorithms for plant feature extraction and parameter computation, ultimately writing the results to the specified output buffer. This process achieves CPU-GPU overlapping computation, GPU pipeline parallelism, and data locality optimization, significantly enhancing vegetation modeling efficiency. The parallel processing architecture of the CRCP algorithm is illustrated in Figure 8.

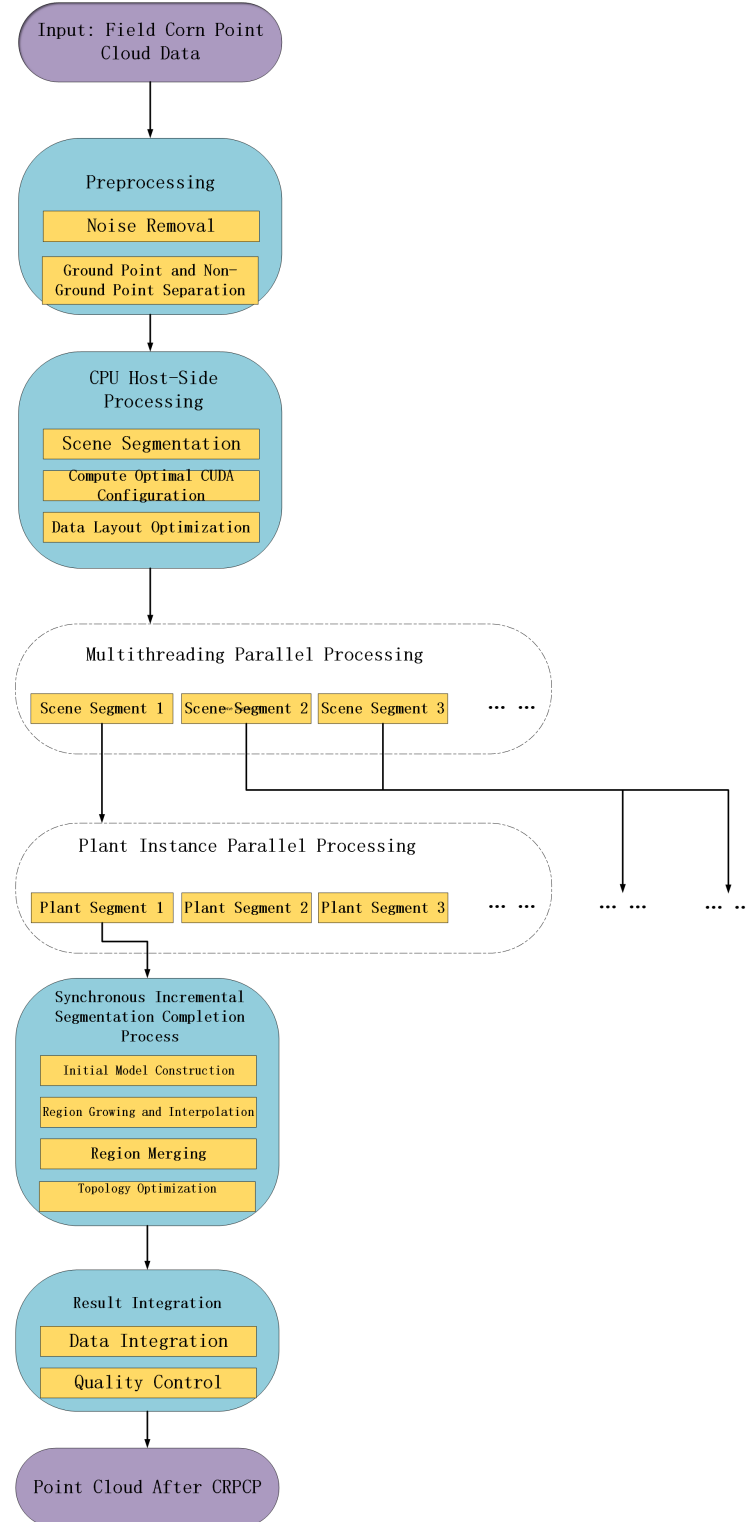


**Figure 8.** Parallel processing architecture diagram for the CRPCP algorithm, with arrows indicating the flow of execution steps.

#### 2.6.3. Data Sharing Optimization within Thread Blocks

The GPU kernel function is modified to allocate threads of the same plant to a single thread block, using shared memory within the block to cache intermediate results generated during steps like RBF interpolation. This approach avoids repeatedly reading intermediate results from global memory, enabling rapid thread communication and access to intermediate results via shared memory, thereby reducing the load on bandwidth-limited global

memory. Optimizing the host-side data layout enhances the spatial locality of point cloud data, increasing the cache hit rate during CPU-to-GPU data transmission. The computational task is divided into multiple sub-processes, including data transmission, segmenting the plant point cloud from the background, calculating features like normals/curvatures, RBF parameter fitting, and result collection. Each sub-process is assigned an independent CUDA stream, with the execution order of each stream coordinated through careful scheduling. First, the data transmission stream is initiated. Once data transmission is complete, the feature extraction stream begins, ensuring effective GPU parallelism and minimizing data transmission overhead.

### 2.7. Calculation of Plant Height

Maize plant height is defined as the vertical distance from the plant's highest point to the ground. Least squares fitting, a commonly used and straightforward method for ground plane fitting, often suffers from noise-induced inaccuracies. The Random Sample Consensus (RANSAC) algorithm iteratively fits data points, effectively eliminating noise and significantly improving fitting accuracy. In the preprocessing stage, outliers in the ground point cloud, identified through color segmentation, are filtered out, followed by the application of the RANSAC algorithm to fit the ground plane equation. To calculate plant height, the maize plant point cloud data are first input into the system. The system then traverses all data points to identify the coordinates of the highest point ( $x, y, z_{max}$ ) and calculates the distance from this point to the ground, thereby determining the maize plant's height. The process of calculating plant height is illustrated in Figure 9.

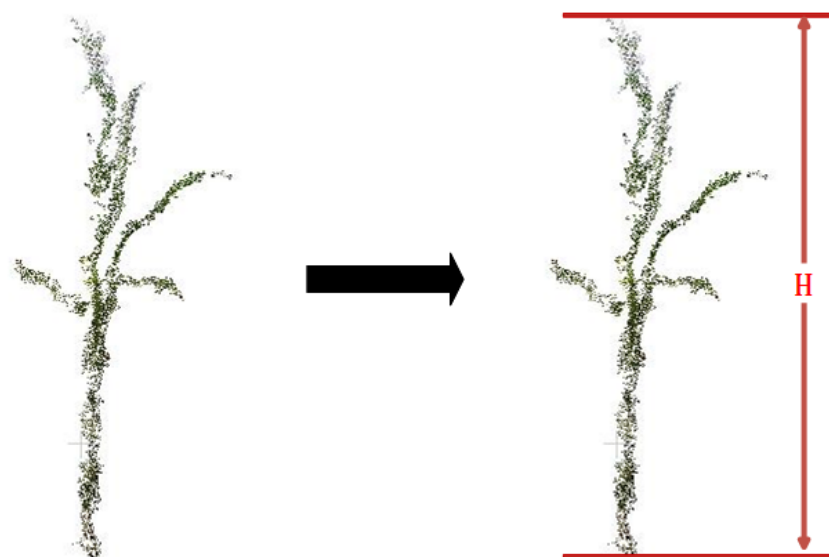


**Figure 9.** Schematic diagram of plant height calculation.

### 2.8. Calculation of Stem Diameter

This study employs an ellipse-fitting method to model the point cloud of the plant geometrically stem cross-section, thereby accurately obtaining the shape and size information of the stem. Specifically, the point cloud data near the target height are initially filtered based on a preset height threshold. The filtered point cloud is subsequently projected onto a two-dimensional plane, disregarding the Z coordinate, with each point represented by ( $X, Y$ ) coordinates. An optimization objective function for ellipse fitting is then constructed to minimize the total distance from the points to the edge of the fitted ellipse, solving for the ellipse parameters. The objective function is as follows:

$$\min_{x_0, y_0, a, b, \theta} \sum_{i=1}^N \left(1 - \frac{u_i^2}{a^2} - \frac{v_i^2}{b^2}\right)^2 \quad (27)$$

where  $u_i = ((x_i - x_0) \cos \theta + (y_i - y_0) \sin \theta)$  and  $v_i = ((x_i - x_0) \sin \theta - (y_i - y_0) \cos \theta)$ , with  $(x_0, y_0)$  representing the coordinates of the ellipse center. Here,  $D = 2a$  and  $b$  denote the lengths of the semi-major and semi-minor axes, respectively,  $\theta$  is the rotation angle, and  $N$  is the number of points. By solving the optimization problem, the parameters of the fitted ellipse are determined, with the estimated stem diameter being twice the length of the semi-major axis ( $D = 2a$ ). The procedure for calculating the stem diameter is illustrated in Figure 10. This algorithm, which utilizes three-dimensional plant point cloud data, effectively determines the elliptical model of the stem cross-section and accurately estimates the stem diameter, thereby providing critical support for subsequent phenotypic parameter extraction.

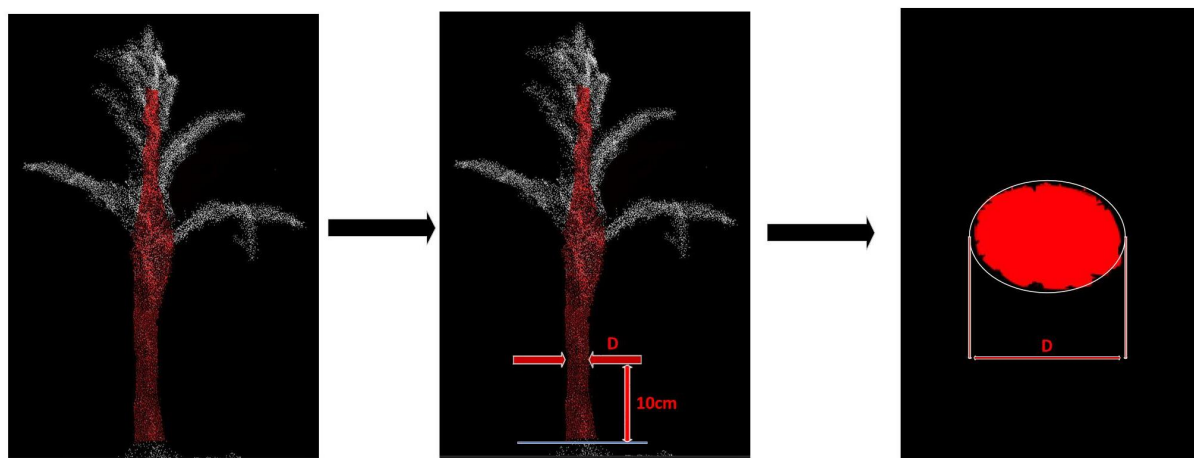


**Figure 10.** Schematic diagram of breast diameter calculation.

### 3. Results

#### 3.1. Segmentation Results of Field Maize Plants

##### 3.1.1. Effect of Similarity Threshold $M$ on Segmentation Granularity

Adjusting the parameter  $M$  achieves a dynamic balance between segmentation quality and computational efficiency in the constrained region growing algorithm. Increasing the value of  $M$  prolongs the growth process, while decreasing it accelerates algorithm convergence, thereby allowing flexible control over the maximum number of regions or growth steps. As demonstrated in Table 1, the segmentation evaluation metrics of the algorithm show significant variations when the parameter  $M$  varies from 0.1 to 0.9. At  $M = 0.5$ , the segmentation accuracy (SA), F1 score, boundary precision (BP), and intersection over union (IoU) achieve their optimal values of 96.2%, 93.8%, 92.6%, and 87.4%, respectively.

**Table 1.** Segmentation metrics for different  $M$  values.

M Value	0.1	0.2	0.3	0.4	0.5	0.6	0.7	0.8	0.9
SA (%)	89.2	91.7	93.5	94.8	96.2	95.1	93.9	92.3	90.6
F1 Score (%)	85.6	88.4	90.7	92.1	93.8	92.5	91.2	89.4	87.1
BP (%)	83.7	86.9	89.3	91.2	92.6	91.8	90.1	88.5	85.9
IoU (%)	79.3	82.6	84.8	86.2	87.4	86.1	84.5	82.4	80.7

Through quantitative analysis, we discovered that as the  $M$  value increases, the segmentation granularity becomes finer, facilitating enhanced capture of surface details and local curvature changes of the stem, as illustrated in Figure 11.

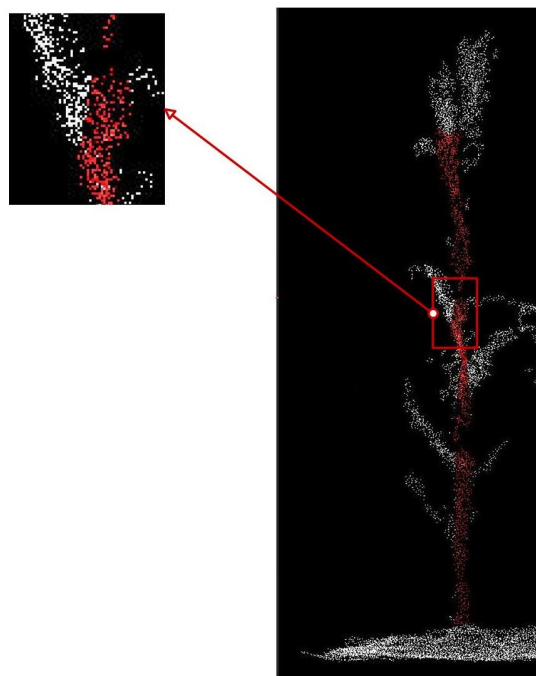


**Figure 11.** Detailed segmentation schematic diagram.

### 3.1.2. Segmented Segmentation Strategy

Considering the complex and heterogeneous structure of the stem, this paper presents a segmented segmentation strategy. This approach involves selecting multiple sets of start and end seed points, enabling the application of suitable segmentation parameters  $M$  and methods tailored to characteristic regions such as nodes and branching points. This ensures that these specialized areas receive more precise and appropriate processing, enhancing overall segmentation accuracy and efficiency.

Figure 12 illustrates the application of this segmented segmentation strategy on a maize plant. Smaller  $M$  values (0.3–0.4) are employed for fine segmentation in node and branching point areas, while relatively larger  $M$  values (0.6–0.7) are utilized for coarser segmentation in the smooth stem regions, effectively balancing segmentation detail and efficiency. As depicted in Figure 13, the algorithm accurately distinguishes different plant individuals and precisely delineates the contours and detailed features of each stem, laying a robust foundation for subsequent measurements and analyses.

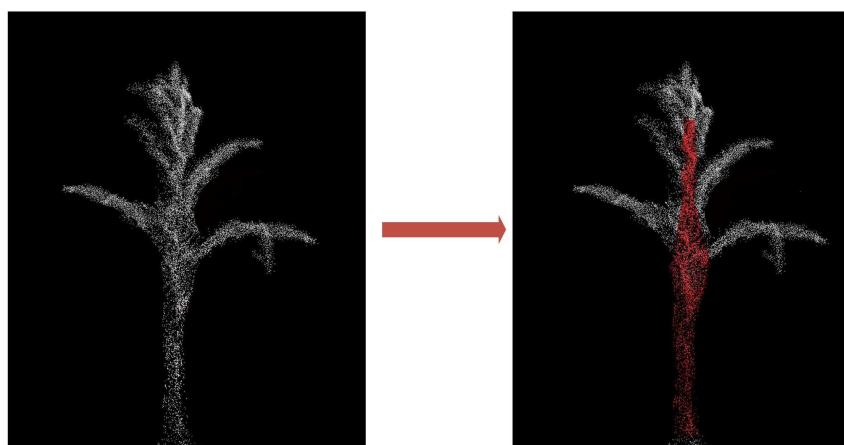


**Figure 12.** Effect of segmented segmentation strategy on a corn plant.

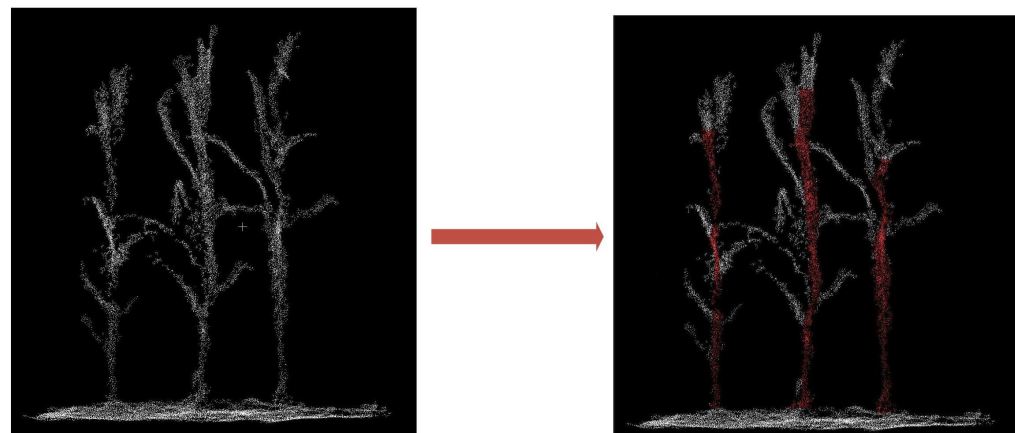


**Figure 13.** Effect of segmented segmentation strategy on multiple corn plants.

### 3.2. Results of Constrained Adaptive Point Cloud Completion Based on Radial Basis Functions

This study assesses completion quality using three standard metrics for point clouds: Point Cloud Completeness (PC), Surface Smoothness (SM), and Resolution Fidelity (RD). As depicted in Table 2, comparing metrics before and after completion reveals an increase in PC from 0.73 to 0.95, SM from 0.86 to 0.97, and RD from 0.69 to 0.91. These results clearly illustrate substantial enhancements in completeness, smoothness, and resolution of the point cloud model post-completion.

**Table 2.** Comparison of point cloud quality metrics before and after completion.

Metric	Before Completion	After Completion
Point Cloud Completeness (PC)	0.73	0.95
Surface Smoothness (SM)	0.86	0.97
Resolution Fidelity (RD)	0.69	0.91

Figure 14 shows a comparison of point clouds of multiple maize plants before and after completion. The completed point cloud has clearer contours and a more complete structure. White points represent the original point cloud data, while red points are the added interpolated points. We also need to estimate the color value for each new interpolated point to ensure a smooth color transition.

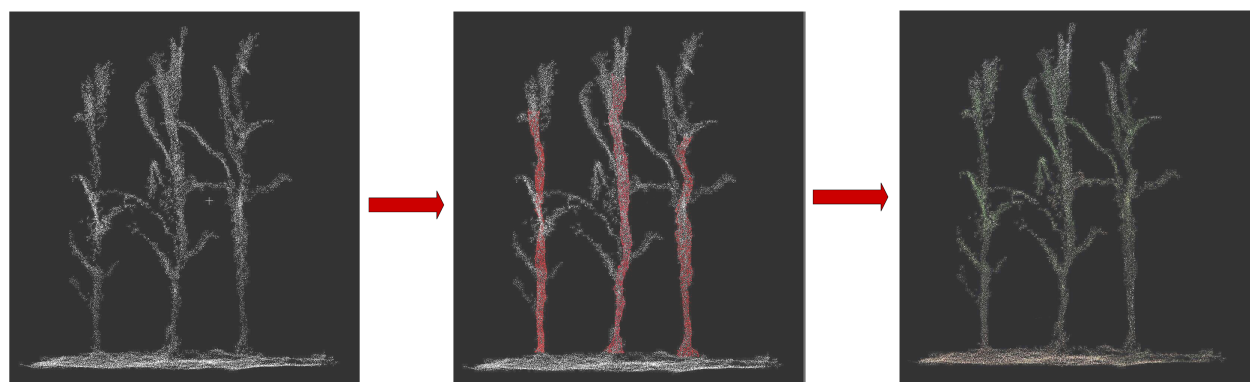


**Figure 14.** Comparison of multiple corn plant point clouds before and after completion.

### 3.3. Results and Analysis of Stem Height and Diameter at Breast Height Measurements

This study employs the RANSAC algorithm to fit the ground plane, enhancing robustness and establishing a foundation for height measurement. To measure height, the algorithm identifies the highest point in the point cloud and calculates its vertical distance from the ground. For diameter at breast height (DBH) measurement, point cloud data

at approximately 0.7 m height are selected and projected onto a two-dimensional plane, followed by cross-sectional modeling using an ellipse-fitting algorithm. Figure 15a presents a scatterplot comparing plant height measurements obtained by the algorithm with manual measurements, achieving a coefficient of determination ( $R^2$ ) of 0.9534 and a root mean square error (RMSE) of 0.4835 cm. Figure 15b displays a scatterplot of DBH measurements obtained by the algorithm, showing a high correlation with manual measurements, indicated by  $R^2$  of 0.9407 and RMSE of 0.0368 cm.

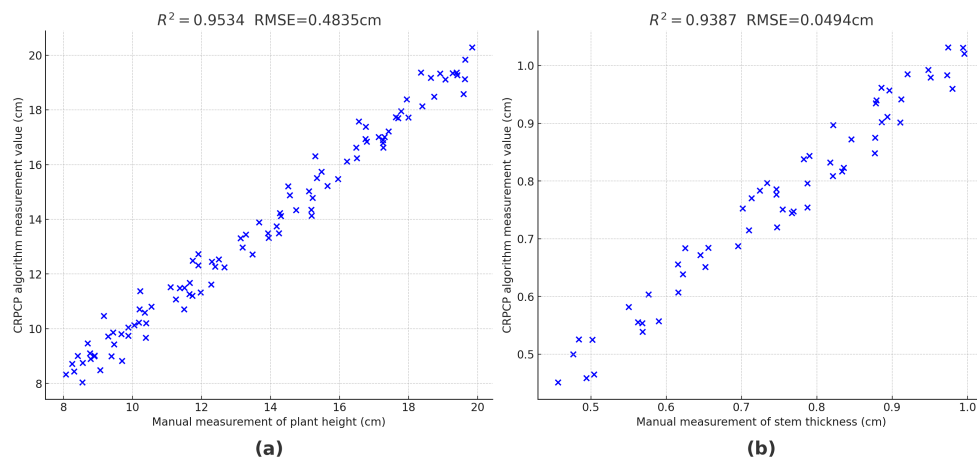


**Figure 15.** (a) Scatterplot of plant height measurements obtained by the algorithm and manual measurements. and (b) Scatterplot of stem-breast diameter measurements obtained by the algorithm and manual measurements.

Table 3 presents a comparison of the accuracy of this method against other traditional measurement techniques. The results indicate that it surpasses voxel estimation, image-based stem side projection, and convolutional neural network-based fitting methods in metrics such as the correlation coefficient, root mean square error, and mean absolute error.

**Table 3.** Comparison of measurement methods.

Method	Correlation Coefficient ( $R^2$ ) (Height/DBH)	RMSE (Height/DBH)	MAE (Height/DBH)
This Method	0.9534/0.9407	0.4835 cm/0.0368 cm	0.3830 cm/0.0310 cm
Voxel Estimation	0.9203/0.9102	0.5803 cm/0.0451 cm	0.4502 cm/0.0403 cm
Stem Side Projection	0.9005/0.8904	0.6302 cm/0.0501 cm	0.5003 cm/0.0432 cm
CNN Fitting	0.9303/0.9201	0.5302 cm/0.0421 cm	0.4201 cm/0.0371 cm

### 3.4. Parallel Computing Results

To validate the effectiveness of the optimization algorithm in practical applications, point cloud datasets of maize plants at various growth stages were collected to assess the accuracy and efficiency of height and DBH measurements. The experimental setup utilized an RTX 4060 GPU and an i5 12400 CPU. Table 4 compares measurement metrics between the CUDA-accelerated algorithm and the CPU serial algorithm across different growth stages. The CUDA algorithm achieves substantial runtime reductions at each stage, demonstrating over 10-fold speedups and highlighting the excellent acceleration capabilities of the parallel computing optimization strategy.

**Table 4.** Comparison of measurement metrics at different growth stages.

Growth Stage	Algorithm	Correlation Coefficient $R^2$	RMSE (cm)	MAE (cm)	Runtime (s)
Seedling Stage	CUDA	0.958	0.52	0.41	2.15
	CPU	0.953	0.57	0.46	35.98
Jointing Stage	CUDA	0.945	0.62	0.49	4.67
	CPU	0.941	0.67	0.54	90.15
Booting Stage	CUDA	0.963	0.48	0.38	9.23
	CPU	0.959	0.53	0.42	197.85
Milk Ripening Stage	CUDA	0.972	0.43	0.35	18.62
	CPU	0.968	0.47	0.37	393.74

## 4. Discussion

### 4.1. Comparison with Other Segmentation Methods

This study presents a comparative analysis of five advanced techniques for measuring the stem diameter at breast height (DBH): (1) the CRPCP algorithm, (2) PointNet, (3) PointNet2, (4) PBNet, and (5) the region-growing algorithm in the Point Cloud Library (PCL). The CRPCP algorithm combines an enhanced region-growing technique with Radial Basis Function (RBF) interpolation to achieve comprehensive results. Notably, PointNet, PointNet2, PBNet, and the region-growing algorithm of PCL are recognized as state-of-the-art methods in the field. For training and evaluation, these deep learning models were trained on the annotated Corn50 public dataset, which includes RGB point cloud models of 50 corn plants. Precise segmentation of corn plant point clouds was achieved by training PointNet, PointNet2, and PBNet with annotated data over 100 iterations. The experimental outcomes (Table 5) include metrics such as overall segmentation accuracy, processing time,  $R^2$  correlation coefficient, RMSE (root mean square error), and MAE (mean absolute error). The CRPCP algorithm achieved an overall segmentation accuracy of 96.2%, surpassing PBNet's 94.5%, PointNet2's 94.2%, PointNet's 93.8%, and the region-growing algorithm of PCL's 91.6%. For DBH measurements, the CRPCP algorithm recorded an  $R^2$  of 0.9407, an RMSE of 0.0368 cm, and an MAE of 0.031 cm, significantly outperforming the other methods.

**Table 5.** Performance comparison of different methods for DBH measurements.

Method	Overall Accuracy (%)	Segmentation Time (s)	Diameter $R^2$	Diameter RMSE (cm)	Diameter MAE (cm)
PCL Region Growing	91.6	15.2	0.9087	0.1320	0.1085
PointNet	93.8	28.9	0.9335	0.5945	0.0597
PointNet2	94.2	24.1	0.9360	0.0522	0.0575
PBNet	94.5	22.3	0.9385	0.0499	0.0453
CRPCP	96.2	16.0	0.9407	0.0368	0.0310

### 4.2. Comparison with Other Complementary Methods

To validate the effectiveness of the Radial Basis Function (RBF) interpolation method in the CRPCP algorithm, we selected 10 maize plant point clouds with data gaps from the dataset for comparative analysis. The evaluation metrics included point cloud completeness (PC), surface smoothness (SM), resolution fidelity (RD), and computation time (CT, in seconds). The comparison methods included Moving Least Squares (MLS), k-nearest neighbors (KNN) interpolation, voxel grid completion (VGC), and natural neighbor interpolation (NNI).

Table 6 presents a comparative analysis of the different interpolation methods across four evaluation metrics. As shown in Table 1, the RBF-based interpolation method in CRPCP excels in three quality metrics, notably achieving a score of 0.97 in surface smooth-

ness. Although natural neighbor interpolation slightly surpassed CRPCP in point cloud completeness (PC) with a score of 0.96, it underperformed in surface smoothness (SM) and resolution fidelity (RD), and its computation time (0.71 s) was longer than CRPCP's (0.52 s). The Moving Least Squares (MLS) method achieved a surface smoothness score nearly equal to CRPCP (0.96) but fell short in the other two metrics and had a longer computation time (0.78 s) than CRPCP. While k-nearest neighbors (KNN) interpolation had a shorter computation time (0.65 s), its overall performance in the quality metrics was inferior to CRPCP. Voxel grid completion slightly outperformed CRPCP in resolution fidelity, reaching 0.92, but had the longest computation time (0.83 s) and underperformed in the other metrics. In conclusion, the RBF interpolation method in the CRPCP algorithm demonstrated an excellent balance of performance in point cloud completion, maintaining high-quality reconstruction and computational efficiency, making it an optimal solution for processing low-density maize point cloud data in outdoor settings.

**Table 6.** Performance comparison of different point cloud completion methods.

Method	PC	SM	RF	CT (s)
CRPCP (RBF)	0.95	0.97	0.91	3.24
MLS	0.91	0.91	0.87	5.67
KNN	0.88	0.91	0.92	4.33
VGC	0.78	0.82	0.87	2.98
NNI	0.89	0.93	0.86	4.19

#### 4.3. Computational Efficiency and Its Applicability to Real-Time Applications

The exceptional computational efficiency of the CRPCP algorithm is crucial for its application in real-time field scenarios. Experimental results in Section 4.1 show that the CUDA-accelerated CRPCP algorithm significantly outperformed the CPU serial algorithm, achieving speedups exceeding 10× across all growth stages. During the more complex milk ripening stage, the CUDA algorithm completed processing in 18.62 s, compared to 393.74 s with the CPU algorithm. This level of efficiency improvement is crucial for real-time applications, enabling rapid acquisition and processing of large-scale plant data in the field.

Compared to other advanced point cloud segmentation methods, the CRPCP algorithm maintains high accuracy (96.2% segmentation accuracy) while reducing processing time by 28.2% to 44.6%. This significant reduction in processing time greatly enhances the algorithm's suitability for real-time scenarios. For example, during rapid breeding screening, researchers can quickly obtain accurate phenotypic data for large numbers of plants, accelerating breeding cycles [31]. In precision agriculture, practitioners can acquire near-real-time crop growth data, enabling timely adjustments to irrigation, fertilization, and other management strategies [32,33].

The algorithm's efficient processing capabilities also enable real-time applications on portable platforms like mobile devices or drones. Given the CRPCP algorithm's robust performance on mid-range hardware (RTX 4060 GPU and i5 12400 CPU), it is likely that relatively fast data processing is achievable on devices with more constrained computational resources, such as tablets with integrated GPUs or high-performance smartphones. This device-level adaptability is critical for agricultural management scenarios that require rapid decision-making, such as early pest detection and drought stress assessment [15].

The high computational efficiency of the CRPCP algorithm lays the foundation for its widespread adoption in real-time field applications. It meets current demands for rapid data processing in precision agriculture and provides technological support for more intelligent and automated agricultural production in the future. As hardware performance improves and the algorithm is further optimized, CRPCP is expected to play a pivotal role in larger-scale and more complex real-time agricultural applications [34,35].

#### 4.4. Limitations and Potential Areas for Future Research

1. Optimization of Computational Efficiency: Although the CRPCP algorithm has achieved significant performance improvements, further optimization is possible. Implementing advanced parallel computing strategies, such as heterogeneous system parallelism, could fully leverage the combined computing power of both CPUs and GPUs, further boosting computational throughput [36]. Additionally, optimizations at the algorithmic and code levels could further enhance computational performance [37,38]. These improvements would enable the processing of larger-scale field data and enhance real-time analysis capabilities [18].

2. Algorithm Robustness: The accuracy of the CRPCP algorithm may be reduced when handling extremely complex and sparse point cloud data. Enhancing the algorithm's robustness and accuracy is crucial for ensuring reliable phenotypic measurements [39]. Optimizing similarity criteria and seed point selection strategies could increase the algorithm's adaptability to complex plant structures and environmental conditions [40]. This would enhance its applicability across different growth stages and crop varieties [27].

3. Multi-source Data Integration: Integrating heterogeneous data, such as RGB images [41], can compensate for the limitations of point cloud data, thereby improving segmentation and completion accuracy [42]. This multi-modal data fusion approach could provide more comprehensive and accurate information for phenotypic measurement in complex agricultural environments, further enhancing the algorithm's adaptability and reliability [28].

4. Expansion of Application Scope: While the CRPCP algorithm has shown excellent performance in maize phenotypic measurement, its applicability to other crops or more complex agricultural scenarios requires further validation [43]. Future research could explore extending this method to other crop varieties or more complex agricultural environments, such as high-density planting or intercropping systems [5].

#### 5. Conclusions

This paper presents a method for obtaining maize phenotypic parameters using the Constrained Region Point Cloud Phenotyping (CRPCP) algorithm. The method first uses a constrained region growth algorithm to segment maize stem point clouds in complex backgrounds, then employs radial basis interpolation to compensate for data loss, and finally implements a multi-level parallel decomposition strategy based on scene blocking and plant instances for high-throughput real-time computation. In maize plant height measurements, the algorithm achieved a correlation coefficient ( $R^2$ ) of 0.9534 compared to manual measurements, with a root mean square error (RMSE) of 0.4835 cm and a mean absolute error (MAE) of 0.383 cm. For stem diameter assessments, the  $R^2$  value was 0.9407, with an RMSE of 0.0368 cm and an MAE of 0.031 cm, demonstrating the algorithm's accuracy and reliability. Compared to the PointNet point cloud segmentation method, the CRPCP algorithm reduced segmentation time by over 44.7%, greatly enhancing analytical efficiency. This highlights the algorithm's accuracy, efficiency, and potential for widespread application in agricultural phenotyping.

This study provides an accurate and efficient method for obtaining phenotypic parameters in maize breeding and cultivation management, supporting the intelligent and modern development of agriculture [44]. In the future, this technology could be extended to measure and analyze phenotypic information at different plant growth stages, establish growth prediction models, and investigate the mechanisms by which environmental factors affect plant growth, providing a scientific basis for crop breeding and cultivation management [45]. In application, this technology could be expanded to farmland monitoring and management [46]. By integrating multi-source data from drones and ground sensors, a complete smart agriculture system could be constructed, enabling real-time monitoring, data analysis, and decision support for agricultural environments [47], thus promoting the intelligent and modern advancement of agricultural production.

**Author Contributions:** Conceptualization, Q.Z. and M.Y.; methodology, Q.Z.; software, M.B.; validation, Q.Z., M.Y. and M.B.; formal analysis, Q.Z.; investigation, Q.Z.; resources, M.B.; data curation, Q.Z.; writing—original draft preparation, Q.Z. and M.Y.; writing—review and editing, Q.Z. and M.B.; visualization, M.B.; supervision, M.Y.; funding acquisition, M.Y. All authors have read and agreed to the published version of the manuscript.

**Funding:** This work was supported by the Key Research and Development Program Heilongjiang Province of China (Grant No. 2022ZX01A35).

**Data Availability Statement:** The data used in this study are available from the corresponding author upon reasonable request.

**Conflicts of Interest:** The authors declare no conflicts of interest.

## References

- Li, Z.; Guo, R.; Li, M.; Chen, Y.; Li, G. A review of computer vision technologies for plant phenotyping. *Comput. Electron. Agric.* **2020**, *176*, 105672. [\[CrossRef\]](#)
- Vågsholm, I.; Arzoomand, N.S.; Boqvist, S. Food security, safety, and sustainability—Getting the trade-offs right. *Front. Sustain. Food Syst.* **2020**, *4*, 16. [\[CrossRef\]](#)
- Viana, C.M.; Freire, D.; Abrantes, P.; Rocha, J.; Pereira, P. Agricultural land systems importance for supporting food security and sustainable development goals: A systematic review. *Sci. Total Environ.* **2022**, *806*, 150718. [\[CrossRef\]](#) [\[PubMed\]](#)
- Beltran-Peña, A.; Rosa, L.; D’Odorico, P. Global food self-sufficiency in the 21st century under sustainable intensification of agriculture. *Environ. Res. Lett.* **2020**, *15*, 095004. [\[CrossRef\]](#)
- Hoogeboom, P. Classification of agricultural crops in radar images. *IEEE Trans. Geosci. Remote Sens.* **1983**, *3*, 329–336. [\[CrossRef\]](#)
- Yang, W.; Feng, H.; Zhang, X.; Zhang, J.; Doonan, J.H.; Batchelor, W.D.; Xiong, L.; Yan, J. Crop phenomics and high-throughput phenotyping: Past decades, current challenges, and future perspectives. *Mol. Plant* **2020**, *13*, 187–214. [\[CrossRef\]](#)
- Sodhi, P.; Vijayaraman, S.; Wettergreen, D. In-field segmentation and identification of plant structures using 3D imaging. In Proceedings of the 2017 IEEE/RSJ International Conference on Intelligent Robots and Systems (IROS), Vancouver, BC, Canada, 24–28 September 2017; pp. 5180–5187.
- Alenya, G.; Dellen, B.; Torras, C. 3D modelling of leaves from color and ToF data for robotized plant measuring. In Proceedings of the 2011 IEEE International Conference on Robotics and Automation, Shanghai, China, 9–13 May 2011; pp. 3408–3414.
- Hu, X.; Zhang, X.; Chen, X.; Zheng, L. Research on Corn Leaf and Stalk Recognition and Ranging Technology Based on LiDAR and Camera Fusion. *Sensors* **2024**, *24*, 5422. [\[CrossRef\]](#)
- Zhao, J.; Chen, S.; Zhou, B.; He, H.; Zhao, Y.; Wang, Y.; Zhou, X. Multitemporal Field-Based Maize Plant Height Information Extraction and Verification Using Solid-State LiDAR. *Agronomy* **2024**, *14*, 1069. [\[CrossRef\]](#)
- Kim, W.S.; Lee, D.H.; Kim, Y.J.; Kim, T.; Lee, W.S.; Choi, C.H. Stereo-vision-based crop height estimation for agricultural robots. *Comput. Electron. Agric.* **2021**, *181*, 105937. [\[CrossRef\]](#)
- Gai, J.; Xiang, L.; Tang, L. Using a depth camera for crop row detection and mapping for under-canopy navigation of agricultural robotic vehicle. *Comput. Electron. Agric.* **2021**, *188*, 106301. [\[CrossRef\]](#)
- Xu, N.; Sun, G.; Bai, Y.; Zhou, X.; Cai, J.; Huang, Y. Global reconstruction method of maize population at seedling stage based on Kinect sensor. *Agriculture* **2023**, *13*, 348. [\[CrossRef\]](#)
- Azzari, G.; Goulden, M.L.; Rusu, R.B. Rapid characterization of vegetation structure with a Microsoft Kinect sensor. *Sensors* **2013**, *13*, 2384–2398. [\[CrossRef\]](#) [\[PubMed\]](#)
- Yang, R.; He, Y.; Lu, X.; Zhao, Y.; Li, Y.; Yang, Y.; Kong, W.; Liu, F. 3D-based precise evaluation pipeline for maize ear rot using multi-view stereo reconstruction and point cloud semantic segmentation. *Comput. Electron. Agric.* **2024**, *216*, 108512. [\[CrossRef\]](#)
- Gao, Y.; Li, Z.; Li, B.; Zhang, L. Extraction of Corn Plant Phenotypic Parameters with Keypoint Detection and Stereo Images. *Agronomy* **2024**, *14*, 1110. [\[CrossRef\]](#)
- Yang, X.; Miao, T.; Tian, X.; Wang, D.; Zhao, J.; Lin, L.; Zhu, C.; Yang, T.; Xu, T. Maize stem-leaf segmentation framework based on deformable point clouds. *ISPRS J. Photogramm. Remote Sens.* **2024**, *211*, 49–66. [\[CrossRef\]](#)
- Lin, C.; Hu, F.; Peng, J.; Wang, J.; Zhai, R. Segmentation and stratification methods of field maize terrestrial LiDAR point cloud. *Agriculture* **2022**, *12*, 1450. [\[CrossRef\]](#)
- Zermas, D.; Morellas, V.; Mulla, D.; Papanikopoulos, N. 3D model processing for high throughput phenotype extraction—the case of corn. *Comput. Electron. Agric.* **2020**, *172*, 105047. [\[CrossRef\]](#)
- Sun, Y.; Guo, X.; Yang, H. Win-Former: Window-Based Transformer for Maize Plant Point Cloud Semantic Segmentation. *Agronomy* **2023**, *13*, 2723. [\[CrossRef\]](#)
- Rivera, G.; Porras, R.; Florencia, R.; Sánchez-Solís, J.P. LiDAR applications in precision agriculture for cultivating crops: A review of recent advances. *Comput. Electron. Agric.* **2023**, *207*, 107737. [\[CrossRef\]](#)
- Miao, Y.; Li, S.; Wang, L.; Li, H.; Qiu, R.; Zhang, M. A single plant segmentation method of maize point cloud based on Euclidean clustering and K-means clustering. *Comput. Electron. Agric.* **2023**, *210*, 107951. [\[CrossRef\]](#)

23. Li, Y.; Wen, W.; Miao, T.; Wu, S.; Yu, Z.; Wang, X.; Guo, X.; Zhao, C. Automatic organ-level point cloud segmentation of maize shoots by integrating high-throughput data acquisition and deep learning. *Comput. Electron. Agric.* **2022**, *193*, 106702. [CrossRef]
24. Guo, R.; Xie, J.; Zhu, J.; Cheng, R.; Zhang, Y.; Zhang, X.; Gong, X.; Zhang, R.; Wang, H.; Meng, F. Improved 3D point cloud segmentation for accurate phenotypic analysis of cabbage plants using deep learning and clustering algorithms. *Comput. Electron. Agric.* **2023**, *211*, 108014. [CrossRef]
25. Jayakumari, R.; Nidamanuri, R.R.; Ramiya, A.M. Object-level classification of vegetable crops in 3D LiDAR point cloud using deep learning convolutional neural networks. *Precis. Agric.* **2021**, *22*, 1617–1633. [CrossRef]
26. Zhu, B.; Zhang, Y.; Sun, Y.; Shi, Y.; Ma, Y.; Guo, Y. Quantitative estimation of organ-scale phenotypic parameters of field crops through 3D modeling using extremely low altitude UAV images. *Comput. Electron. Agric.* **2023**, *210*, 107910. [CrossRef]
27. Xu, Y.; Tong, X.; Stilla, U. Voxel-based representation of 3D point clouds: Methods, applications, and its potential use in the construction industry. *Autom. Constr.* **2021**, *126*, 103675. [CrossRef]
28. Lv, C.; Lin, W.; Zhao, B. Approximate intrinsic voxel structure for point cloud simplification. *IEEE Trans. Image Process.* **2021**, *30*, 7241–7255. [CrossRef]
29. Li, Z.; Shan, J. RANSAC-based multi primitive building reconstruction from 3D point clouds. *ISPRS J. Photogramm. Remote Sens.* **2022**, *185*, 247–260. [CrossRef]
30. Yang, L.; Li, Y.; Li, X.; Meng, Z.; Luo, H. Efficient plane extraction using normal estimation and RANSAC from 3D point cloud. *Comput. Stand. Interfaces* **2022**, *82*, 103608. [CrossRef]
31. Singh, A.K.; Ganapathysubramanian, B.; Sarkar, S.; Singh, A. Deep learning for plant stress phenotyping: Trends and future perspectives. *Trends Plant Sci.* **2018**, *23*, 883–898. [CrossRef]
32. Jay, S.; Rabatel, G.; Hadoux, X.; Moura, D.; Gorretta, N. In-field crop row phenotyping from 3D modeling performed using Structure from Motion. *Comput. Electron. Agric.* **2015**, *110*, 70–77. [CrossRef]
33. Ao, Z.; Wu, F.; Hu, S.; Sun, Y.; Su, Y.; Guo, Q.; Xin, Q. Automatic segmentation of stem and leaf components and individual maize plants in field terrestrial LiDAR data using convolutional neural networks. *Crop J.* **2022**, *10*, 1239–1250. [CrossRef]
34. Xiao, Q.; Bai, X.; Zhang, C.; He, Y. Advanced high-throughput plant phenotyping techniques for genome-wide association studies: A review. *J. Adv. Res.* **2022**, *35*, 215–230. [CrossRef] [PubMed]
35. Song, P.; Wang, J.; Guo, X.; Yang, W.; Zhao, C. High-throughput phenotyping: Breaking through the bottleneck in future crop breeding. *Crop J.* **2021**, *9*, 633–645. [CrossRef]
36. Zhai, Z.; Zhu, Z.; Du, Y.; Song, Z.; Mao, E. Multi-crop-row detection algorithm based on binocular vision. *Biosyst. Eng.* **2016**, *150*, 89–103. [CrossRef]
37. Luo, S.; Liu, W.; Zhang, Y.; Wang, C.; Xi, X.; Nie, S.; Ma, D.; Lin, Y.; Zhou, G. Maize and soybean heights estimation from unmanned aerial vehicle (UAV) LiDAR data. *Comput. Electron. Agric.* **2021**, *182*, 106005. [CrossRef]
38. Xie, T.; Li, J.; Yang, C.; Jiang, Z.; Chen, Y.; Guo, L.; Zhang, J. Crop height estimation based on UAV images: Methods, errors, and strategies. *Comput. Electron. Agric.* **2021**, *185*, 106155. [CrossRef]
39. Miao, Y.; Peng, C.; Wang, L.; Qiu, R.; Li, H.; Zhang, M. Measurement method of maize morphological parameters based on point cloud image conversion. *Comput. Electron. Agric.* **2022**, *199*, 107174. [CrossRef]
40. Malachy, N.; Zadak, I.; Rozenstein, O. Comparing methods to extract crop height and estimate crop coefficient from UAV imagery using structure from motion. *Remote Sens.* **2022**, *14*, 810. [CrossRef]
41. Qiu, R.; Miao, Y.; Zhang, M.; Li, H. Detection of the 3D temperature characteristics of maize under water stress using thermal and RGB-D cameras. *Comput. Electron. Agric.* **2021**, *191*, 106551. [CrossRef]
42. Gao, M.; Yang, F.; Wei, H.; Liu, X. Individual maize location and height estimation in field from uav-borne lidar and rgb images. *Remote Sens.* **2022**, *14*, 2292. [CrossRef]
43. Tang, Q.; Zhang, R.; Yi, T.; Xu, G.; Li, L.; Chen, L. Numerical simulation of agricultural unmanned helicopter corn canopy spraying. *Comput. Electron. Agric.* **2024**, *224*, 109178. [CrossRef]
44. Fu, X.; Jiang, D. High-throughput phenotyping: The latest research tool for sustainable crop production under global climate change scenarios. In *Sustainable Crop Productivity and Quality Under Climate Change*; Elsevier: Amsterdam, The Netherlands, 2022; pp. 313–381.
45. Velesaca, H.O.; Mira, R.; Suárez, P.L.; Larrea, C.X.; Sappa, A.D. Deep learning based corn kernel classification. In Proceedings of the IEEE/CVF Conference on Computer Vision and Pattern Recognition Workshops, Seattle, WA, USA, 14–19 June 2020; pp. 66–67.
46. Wei, W.; Yang, T.I.; Rui, L.; Chen, C.; Tao, L.; Kai, Z.; Sun, C.m.; Li, C.y.; Zhu, X.k.; Guo, W.s. Detection and enumeration of wheat grains based on a deep learning method under various scenarios and scales. *J. Integr. Agric.* **2020**, *19*, 1998–2008.
47. Wang, D.; Song, Z.; Miao, T.; Zhu, C.; Yang, X.; Yang, T.; Zhou, Y.; Den, H.; Xu, T. DFSP: A fast and automatic distance field-based stem-leaf segmentation pipeline for point cloud of maize shoot. *Front. Plant Sci.* **2023**, *14*, 1109314. [CrossRef] [PubMed]

**Disclaimer/Publisher's Note:** The statements, opinions and data contained in all publications are solely those of the individual author(s) and contributor(s) and not of MDPI and/or the editor(s). MDPI and/or the editor(s) disclaim responsibility for any injury to people or property resulting from any ideas, methods, instructions or products referred to in the content.